EAI Endorsed Transactions
on Energy Web
Research Article EAI.EU

Design of a Live-Line Inspection Robot System for Insulators in UHVDC Transmission Lines

Yunfeng Yan*, Hao Sun, Fei Hao, Peng Chen, Tianlong Zhang, Zehua Yang

Inner Mongolia Power Group Wuhai Extra High Voltage Power Supply Company, Wuhai, 016000, Inner Mongolia, China

Abstract

To address the pain points of low-zero insulators in UHVDC transmission lines, which are prone to insulation flashover, and the low accuracy, reliance on manual labor, and weak anti-interference capabilities of traditional inspection methods, this study developed an integrated live-line inspection robot that combines mechanical climbing, precise inspection, intelligent control, and electromagnetic shielding. The robot system comprises a mechanical system (tracked movement mechanism, guiding and clamping mechanism), detection system (2500V high-voltage detection circuit, MEGA128 microcontroller control), control system (L298N motor drive, frequency-hopping spread spectrum wireless data transmission), and electromagnetic shielding system (multi-layer shielding shell, opto-isolation, multi-point common ground). An innovative "equipotential bypass" detection principle is proposed to eliminate leakage current interference, and an improved PSO-SVR fusion algorithm is introduced to optimize the detection data. Experimental verification showed that in laboratory tests, the robot exhibited excellent electromagnetic interference resistance (shielding effectiveness SE≥ 60 dB) and a resistance measurement error ≤±2.5%. In actual live-line testing of 500 kV/1000 kV lines, the detection error was ≤±3%, the detection cycle for a single string (28/32 pieces) was only 92~108s, the detection rate of degraded insulators was 100%, and it eliminated the need for power outages and manual tower climbing. This robot meets the "live-line, accurate, efficient, and interference-resistant" detection requirements of UHV lines, providing reliable technical support for the intelligent operation and maintenance of power grids and has broad engineering application prospects.

Keywords: UHVDC transmission; low zero-value insulators; detection robot; PSO-SVR algorithm; live-line detection; electromagnetic shielding; data optimization.

Received on 05 October 2025, accepted on 15 November 2025, published on 09 February 2026

Copyright © 2026 Yunfeng Yan *et al.*, licensed to EAI. This is an open access article distributed under the terms of the CC BY-NC-SA 4.0, which permits copying, redistributing, remixing, transformation, and building upon the material in any medium so long as the original work is properly cited.

doi: 10.4108/ew.11877

1. Introduction

With the deepening of China's energy structure transformation and the "West-to-East Power Transmission" strategy, UHVDC transmission technology has become a core support for cross-regional power dispatch owing to its advantages, such as a large transmission capacity, low loss, and long distance. Currently, UHVDC lines at voltage levels such as ±800 kV have achieved large-scale operation in China, and their safety and stability are crucial for ensuring national economic development and electricity supply for the livelihoods of the people. Insulators, as the core component of the UHVDC line insulation system, bear the dual functions of supporting the conductor and isolating the ground potential; a single line may use tens of thousands of insulators [1]. However, during long-term operation, insulators are susceptible to the combined effects of the natural environment (such as wind and rain erosion and industrial pollution), mechanical stress (conductor self-weight and icing load), and manufacturing defects (uneven adhesive ratio and internal porosity of porcelain components), gradually leading to insulation performance degradation and the formation of "insulators"—that is, insulation resistance dropping below 300MΩ (low value) or approaching zero (zero value). The

*Corresponding author. Email: bj2008_zl@163.com

presence of such insulators significantly alters the voltage distribution of the insulator string, causing the adjacent normal insulators to experience overvoltage [2]. When the insulation margin is insufficient, it can easily trigger surface flashover accidents, causing unplanned power grid outages. According to statistics, in the past five years, UHVDC line faults caused by insulators have accounted for 18% of all faults in China, with economic losses exceeding 10 million Yuan per outage [3]. Therefore, the development of precise insulator testing technology suitable for field conditions has become urgent in the field of UHV power grid operation and maintenance.

To address the challenges of insulator inspection, scholars and engineers have conducted extensive research both domestically and internationally [4]. Existing methods can be broadly categorized into indirect and direct inspections. Among the indirect methods, observation involves manually or via drones visually inspecting the insulator surface for damage and contamination; however, this only identifies external insulation defects and cannot determine internal insulation degradation. Ultrasonic testing utilizes the propagation characteristics of sound waves to identify internal cracks; however, it is easily affected by wind and corona noise, resulting in a low signal-to-noise ratio (SNR). Ultraviolet imaging and infrared thermography identify degradation by capturing corona discharge or temperature anomalies on the insulator surface; however, the equipment cost can reach hundreds of thousands of yuan, and these methods are significantly affected by temperature, humidity, and sunlight intensity, with a detection rate of less than 60% for early stage insulators [5]. Although direct detection methods can directly obtain insulation resistance parameters, they have significant limitations that must be considered. The spark fork method relies on manual handheld operation and judges the degradation state based on the sound of discharge, which is highly subjective and has low accuracy. The leakage current detection method requires sensors connected in parallel at both ends of the insulator string; however, the strong electric field and electromagnetic interference in the field can cause fluctuations in the detection data, making it difficult to accurately distinguish between normal and abnormal insulators [6]. Traditional insulation resistance measurement methods, although highly accurate, require power outages on the line, which not only affect power supply reliability but also pose a risk of falling from heights due to manual tower climbing. In recent years, some research has attempted to develop detection robots; however, existing equipment is mostly focused on AC lines and has not been optimized for insulation protection in the strong electric field environment of UHVDC lines. Furthermore, they generally suffer from weak resistance to leakage current interference and low detection efficiency, failing to meet the on-site requirements of "energized, accurate, and efficient" detection.

Recent studies have made progress in UHVDC live-line inspection but still face critical limitations. Xu et al. (2023) developed a magnetic adsorption robot for UHVDC lines, but its adaptability to double-strand insulator strings is poor, and the detection error (±4.5%) exceeds industrial requirements [7]. Chang et al. combined UAVs with AI image recognition for insulator inspection, but this method only identifies external defects (not insulation resistance) and has an early degradation detection rate of 72% [8]. Riba, J.-R used improved electric field sensors for equipotential detection, but corona interference reduces the signal-to-noise ratio (SNR) to 20dB in strong electric fields [9]. Imdadullah et al. designed a lightweight robot for 1000kV UHVAC lines, but the lack of electromagnetic shielding leads to poor stability in UHVDC environments (shielding effectiveness SE=45dB) [10]. Wen et al. applied random forest for data optimization, but the nonlinear fitting error (±4%) is higher than practical needs [11]. A recent review emphasized that current robots lack efficiency and anti-interference capabilities, highlighting the need for integrated solutions [12]. There is an urgent need to propose new technical solutions to address this gap.

Therefore, this study focuses on the live-line detection of UHVDC line insulators and develops an integrated robot system that combines mechanical climbing, precise detection, and intelligent control to achieve this goal [13]. This study begins by analyzing the insulator degradation mechanism and the changing patterns of its electrical characteristics, providing a theoretical basis for designing the detection principle. Subsequently, addressing the core requirements of "equipotential operation" and "interference resistance," the integrated design of the robot's mechanical structure (including climbing arms, insulating rods, and detection pointers) and control system (including power supply, data acquisition, and communication modules) was completed [14]. An innovative "equipotential bypass" detection method is proposed to eliminate leakage current interference. Simultaneously, a discrete data fitting algorithm based on the least-squares method was introduced to further improve measurement accuracy. Finally, the detection accuracy, efficiency, and stability of the robot were verified through laboratory non-energized tests and on-site energized tests on the UHVDC lines. The research results aim to solve the pain points of traditional detection methods, achieve accurate online detection and early warning of UHVDC line insulators, and provide technical support for the intelligent operation and maintenance of UHVDC power grids. The related design ideas can also serve as a reference for the development of detection robots for other high-voltage equipment.

2. System Design

The insulator string inspection robot can operate on suspended and horizontal double-strand insulator strings with a maximum voltage level of 500 kV. It can perform live-line work, such as visible light detection and resistance measurement, and comprehensively evaluate the operating status of the insulators [15]. This is of great significance for improving the automation level of live-line work and ensuring the safety of the power grids. From a system perspective, an insulator string inspection robot includes mechanical, control, and detection systems. The mechanical

system enables the robot to move back and forth on the insulator strings reliably, quickly, and stably. The detection system performs live-line work, such as visible-light detection and resistance measurements. The control system enables remote control of the robot and the analysis and storage of measurement data. The entire machine can operate safely and stably in an environment with a maximum voltage of 500 kV (Figure 1).

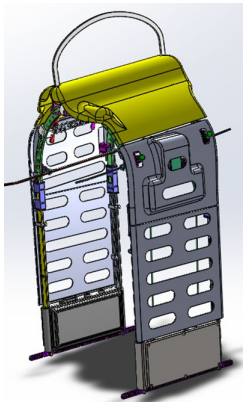

Figure 1. Insulator String Inspection Robot

2.1 Mechanical System Design

The mechanical system of the insulator string inspection robot was designed, including a tracked movement mechanism, guiding and clamping mechanisms, and an inspection mechanism. This system enables the robot to reciprocate reliably, quickly, and stably on both suspended and horizontal double-stranded insulator string. The tracked movement mechanism includes two supports, synchronous pulleys, and a synchronous belt. The synchronous pulleys can rotate synchronously about their axes. Two synchronous belt rollers were installed at the ends of the supports. Because the synchronous belt is in close contact with the insulators, the synchronous belt material was selected as an insulating material for the proposed sensor [16]. The tracked movement mechanism uses ethylene propylene rubber, which is resistant to ozone, has excellent weather resistance, is resistant to water and steam, and has good insulation properties. The motor was connected to a small gear that transmitted power to the movement mechanism located on the same side as the large gear. The synchronous belt then drives the synchronous pulley on the other side, thus completing the power transmission and ensuring synchronous rotation of the track. The actual power of the selected motor was 30 W, which satisfied the requirements. The other main parameters of the motor were as Table 1:

Table 1. Motor Parameters of the Cross Movement Mechanism

Project	Parameter
Voltage	DC12V
Rated Current	1.3A
No-load Speed	17r/min
Load Speed	13r/min
Output Torque	42kg·cm

To ensure reliable movement and insulation performance, key components of the mechanical system are supplemented with detailed parameters:

Tracked Movement Mechanism: The synchronous belt (material: ethylene propylene rubber) has a width of 50mm, thickness of 8mm, and friction coefficient $\geqslant$0.8 to prevent slipping on insulator surfaces. The support structure is made of aluminum alloy 6061, with a length of 350mm and weight of 2.8kg, balancing structural rigidity and lightweight design. The synchronous pulleys (diameter: 60mm, tooth number: 24) maintain a 1:1 transmission ratio to ensure consistent movement of both sides.

Guiding and Clamping Mechanism: Two laser limit sensors (model: KEYENCE IL-1000, detection distance: 0-100mm, accuracy: ±0.1mm) are mounted on the sled-like guide rods to real-time monitor the robot's alignment with insulators, avoiding offset during movement. Four pressure sensors (model: FSR402, detection range: 0-100N, response time: <10ms) are embedded in the clamping jaws to control the gripping force within 30-50N—this range ensures stable attachment without damaging insulator surfaces.

Inspection Mechanism: The detection probes (material: brass with epoxy insulating coating, diameter: 12mm, stroke: 50mm) are driven by a micro motor (model: RS-380SH, rated voltage: 12V, rated speed: 3000rpm) to achieve ±0.5mm positioning accuracy when contacting insulator fittings.

The robot uses a wrapping motion around the insulator. The robot has two hinge points with an opening on the underside to facilitate fitting the robot onto the insulator string, as shown in Figure 2a. The robot has two sled-like guide rods that guide it during movement; these rods are made of insulating materials to ensure insulation and prevent scratching of the insulator [17]. The clamping mechanism provides the robot with a gripping force to keep it firmly attached to the insulator, as shown in Figure 2b. Gravity allows the robot to securely grip an insulator string.

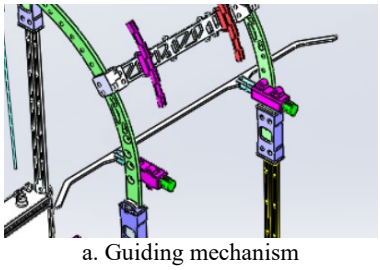

a. Guiding mechanism

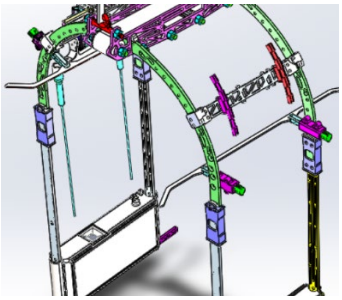

b. Clamping structure

Figure 2. Machine structure for a ring insulator

Epoxy materials are highly compatible with the guiding and clamping mechanisms of insulator inspection robots, with core advantages reflected in five key characteristics and excellent durability. Their density is only 1.5-2.0 g/cm³ (approximately 1/4 that of steel), and their tensile strength reaches 300-800 MPa. This lightweight yet strong characteristic reduces the weight of the mechanism while ensuring its structural rigidity. The mechanical properties can be flexibly controlled by the fiber type, laying method, and resin ratio, thereby balancing the rigid support with flexible adaptation. Their stable molecular structure is water- and acid/alkali-resistant, preventing corrosion [18]. Their volume resistivity is $>10^{14}$ Ω·cm, ensuring that their insulation properties match those of insulators and eliminating the risk of electrical conductivity. The flexible molding process allows for the precise fabrication of complex curved surfaces with a dimensional shrinkage rate of <1%, thereby reducing manufacturing costs. After UV-resistant modification, this material retained >80% of its mechanical properties after 5 years of outdoor exposure. It is not prone to cracking under temperature cycling from -40 to 60℃, exhibits <1% performance degradation after 100,000 cycles, and shows <0.1% dimensional change under humidity variations. With a practical application lifespan of 5-8 years, it is an ideal choice for guiding and clamping mechanisms, effectively ensuring stable robot operation.

2.2 Detection System Design

The resistance measurement method involves applying a high DC voltage to the insulator under test, collecting the leakage current flowing through it, and calculating the insulation resistance using the voltmeter-ammeter method. The detection device mainly consists of a central processing unit, a power management unit, and detection probes. The power management unit includes an output power supply, a boost circuit, and a bypass capacitor. Triggered by the central processing unit, the voltage provided by the output power supply was converted into a DC high voltage of over 2500V via the boost circuit and applied to the detection probes [19]. After the probes contact the upper and lower fittings of the insulator under test, the detection current generated by the insulator under high voltage is transmitted to the central processing unit (CPU) via an acquisition circuit. The insulation resistance value was then calculated through processing and analysis. The main circuit is illustrated in Figure 3. The boost circuit consists of an input power supply, oscillator, transformer, voltage doubler rectifier circuit, and output circuit. This is triggered by the P0.1 pin of the central processing unit. The input power supply powers the oscillator via a voltage regulator module, MCT7805CT. The generated AC signal is boosted to approximately 1000V by a transformer, and then rectified and amplified by a voltage doubler rectifier circuit containing diodes D2-D5 and capacitors C13/C20. Finally, the output circuit delivers approximately 2500V DC high voltage to the detection probe. To ensure electrical safety, large-capacity resistors R6-R9 were connected in series internally to enhance the insulation strength and creepage distance, preventing equipment damage or flashover accidents. Additionally, bypass capacitors C21/C22 were added to effectively bypass the AC voltage of the insulator, eliminating interference and ensuring the detection accuracy.

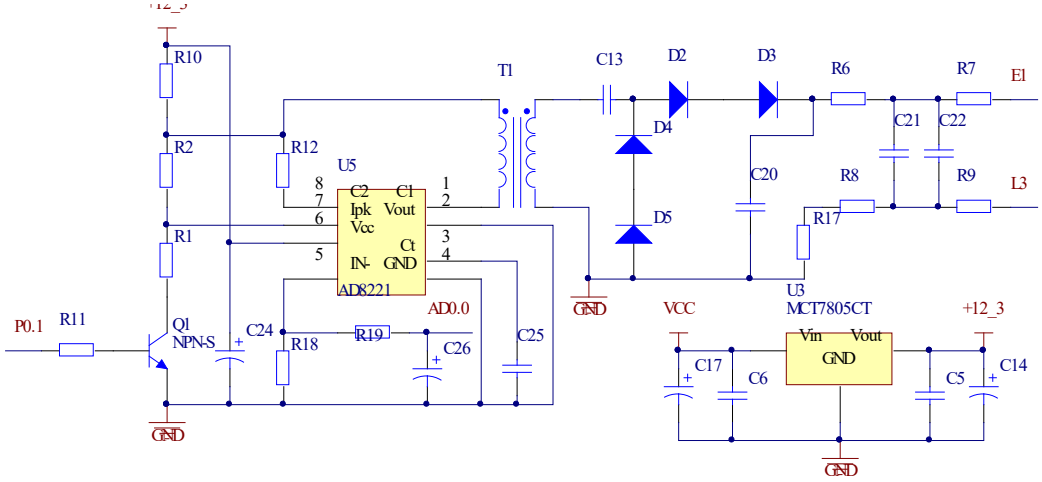

Figure 3. Boost Circuit

The principle of the circuit is illustrated in Figure 4. The acquisition circuit detects the voltage and leakage current. It consists of acquisition resistors R15 and R16 and a voltage follower composed of LM358D. The data output terminals were connected to the central processing unit AD0.0 (voltage acquisition terminal) and AD0.1 (current acquisition terminal). The voltage follower can realize signal isolation and buffering to avoid interference at the acquisition terminals [20]. To ensure safety and save power, the central processing unit adds an induction trigger circuit that senses the power frequency voltage of the analog input port through the AD port. When the detection device is close to the insulator, P0.1 outputs a low level to trigger the boost circuit to work; when it is not close, it outputs a high level to stop the boost circuit, preventing personal injury or line safety accidents caused by the detection probe approaching the line.

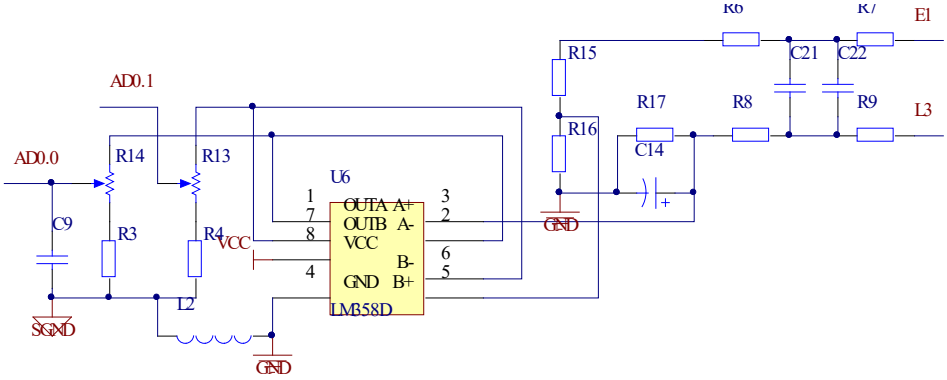

Figure 4. Data Acquisition Circuit

The central processing unit uses a MEGA128 microcontroller. Its main functions include power frequency voltage sensing, boost circuit triggering, analog signal acquisition, data storage, data transmission, and control command reception and parsing. The program flow is shown in Figure 5. The robot body was equipped with a limit switch. Each time the robot slides past an insulator, the limit switch outputs a signal [21]. When the limit switch is active, the robot's main controller controls the detection device motor, causing the probe to contact the upper and lower fittings of the insulator and send a detection command to the detection device via the RS232 interface. Upon receiving the detection command, the detection device begins acquiring data, calculating the resistance, and sending the detection data to the robot's main controller via the RS232 interface. Finally, the main controller of the robot transmits the detection results to the ground receiving device via a wireless data transmission system.

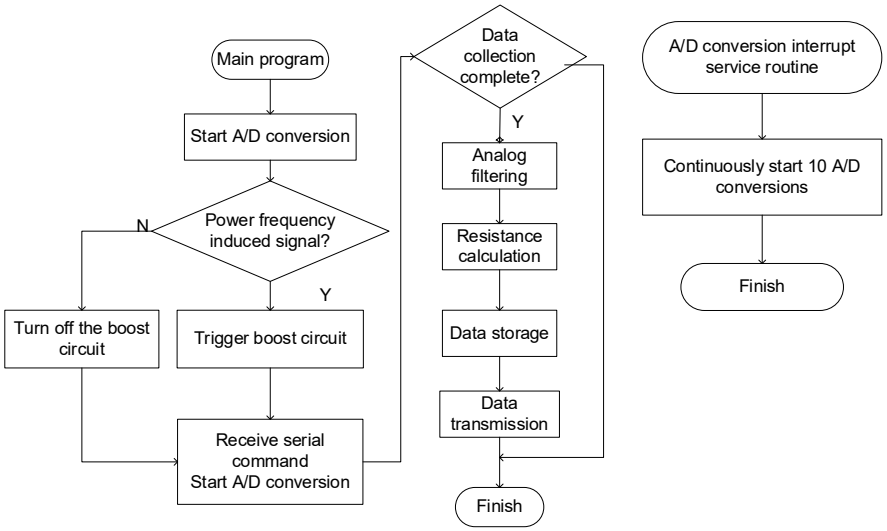

Figure 5. Flowchart of Resistance Detection Program

2.3 Control System Design

As shown in Figure 6, the insulator detection robot control system mainly consists of a remote-control system and a robot body control system. The MCU of the remote control collects signals from the analog joystick and digital buttons, performs the necessary digital filtering on these signals, assembles them into data packets according to a certain protocol, and sends them to the data transmission receiving module of the robot via the wireless data transmission module. The LCD of the remote control displays the real-time data transmission and reception status and battery level information. The robot receives control signals from the remote control, analyzes and processes them, and completes the corresponding actions [22]. The robot can operate entirely in manual mode, meaning that its start-up, stopping, and detection actions are entirely controlled by the remote control. It can also perform fully autonomous detection with the help of laser sensors and proximity switches.

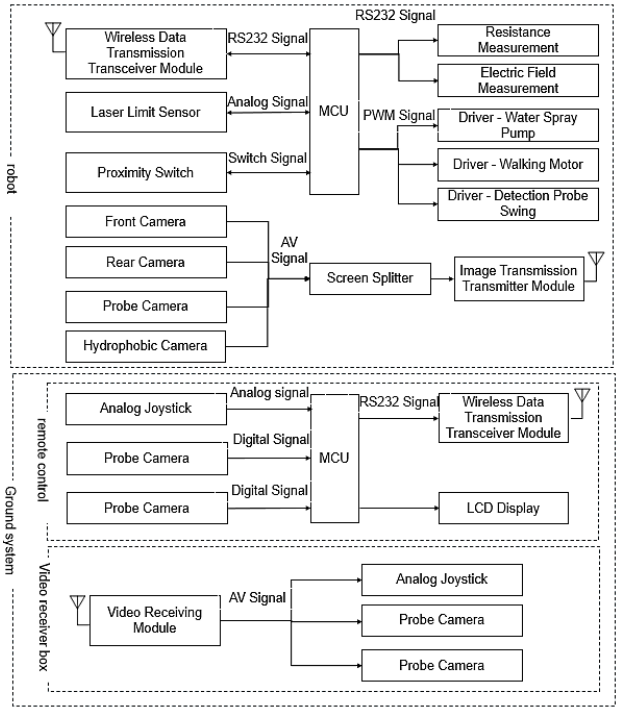

Figure 6. Control System Structure

Motor Control System Design

The low-power motors (drive motor 24 V/15 W, micro pump 24 V/20 W) of the insulator string detection robot were driven by an H-type full-bridge circuit. The SGS L298N driver chip in a 15-pin Multiwatt package was selected, which contains four channels of logic drive circuitry capable of driving two DC motors. The maximum output voltage was 50V, supporting the power regulation output and microcontroller I/O port signal control. The circuit is simple and easy to use in practice. The DC motor speed satisfies the formula n=(U-IR)/Kφ (where U is the armature terminal voltage, I is the armature current, R is the total armature resistance, φ is the magnetic flux per pole, and K is the structural parameter). A widely used armature voltage control method is used for speed regulation. The core solution is PWM speed control based on power electronics technology [23]. The speed is controlled by switching the power supply on and off at a fixed frequency and adjusting the on-off time ratio within the cycle to change the armature voltage. This method has no shock during start-up and shutdown, low power consumption during start-up, and stable operation, making it suitable for robot drive requirements.

Key Sensors for Control

- Laser distance sensor (model: HC-SR04, detection range: 2-400cm) for autonomous navigation, enabling the robot to avoid obstacles on insulator strings.
- Proximity switch (model: TL-N5ME1, detection distance: 0-5mm) for insulator position positioning, triggering detection actions when the robot aligns with each insulator.

Electric field sensor (model: EFS-100, detection range: 0-50kV/m, accuracy: ±1%) for equipotential operation monitoring, ensuring the robot stays in a safe electric field range.

Motor Control Algorithm

The PWM speed regulation adopts a 20kHz signal with a 10%-90% duty cycle (adjustment step: 1%) for stepless speed change. A proportional-integral (PI) controller (proportional gain Kp=0.8, integral gain Ki=0.2) is applied for speed closed-loop control, limiting speed fluctuation to $\leqslant \pm 3\%$ and ensuring stable movement.

Servo Motor Parameters

The pan-tilt servo motor (model: SG90, operating voltage: 4.8-6V, torque: 2.5kg·cm, angle range: 0-180°, response time: <0.1s) uses timer T1 (clock frequency: 16MHz) for interrupt control. The 20ms period is divided into 100 short interrupts (200μs each) to simplify hardware and improve control accuracy.

Filtering Algorithm Implementation

- For analog joystick signals: 10 consecutive samples are collected, 3 maximum and 3 minimum values are removed, and the average of the remaining 4 samples is calculated as the effective value (median averaging filtering, N=10, m=3).
- For switch signals: A debounce filter with a counter (sampling interval: 10ms, threshold Nd=3) is used—only when 3 consecutive consistent samples are detected, the signal is confirmed valid, eliminating switching jitter.

Servo Motor Control System Design

Owing to its large weight, torque, and controllable output angle and speed, a servo motor was used to realize the pan-tilt movement of the camera. Its working principle is as follows: the control signal obtains a DC bias voltage through a modulation chip, which is compared with the internal

reference circuit (20ms period, 1.5ms width reference signal) and the potentiometer voltage to output a voltage difference, driving the motor to rotate forward and backward; the motor drives the potentiometer to rotate through a reduction gear until the voltage difference is 0, at which point it stops. The system adopts a microcontroller timer interrupt control scheme, dividing the 20ms period into short and long interrupts, which simplifies the hardware circuit, reduces software overhead, and improves control efficiency and accuracy. A PWM signal is generated by modifying the initial value of the timer, such as outputting a 2ms high level and an 18ms low level at the left extreme position, which cycles repeatedly to achieve drive. Adjusting the pulse width allows for flexible control of the servomotor movement. To avoid program conflicts, the signal acquisition function was executed in a long timer interrupt, maintaining a 20ms execution cycle to ensure the stable operation of the interrupt program.

Remote Control System Design

The remote control system for the green-string-detection robot is shown in Figure 7. The analog joystick of the remote control uses analog signal acquisition (different states of the toggle switch correspond to different analog quantities), and the reliability of the acquisition is improved through multiple anti-interference design.

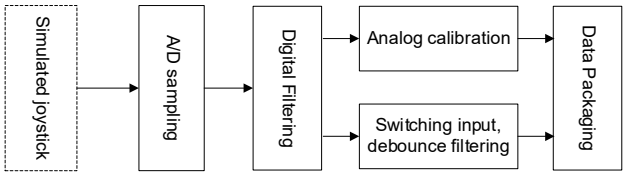

Figure 7. Remote Control System Structure

Both the analog joystick and the switching input used median averaging filtering (N=10, m=3), and the filtered output was:

$$\bar{U}_f = \frac{1}{N-2m}\sum_{i=m+1}^{N-m} w_i U_{(i)} + k_f \Delta U_{ref} \quad (1)$$

In the formula, w_i is the sampling value weight coefficient ($\sum_{i=m+1}^{N-m} w_i = 1$), $U_{(i)}$ is the sorted sampling value, k_f is the filter correction factor, and ΔU_{ref} is the reference deviation. The analog joystick acquisition quantity was linearly corrected to the range of 00~FF, and the correction formula is:

$$U_c = k_c(U_s - U_{s0}) + U_{c0} \quad (2)$$

where k_c is the scaling factor, $U_s$is the original sampling value, U_{s0} is the reference offset, and U_{c0} is the correction starting value. The switch quantity is added with a debouncing filter, and the counter update rule is as follows:

$$C_n = \begin{cases} 0, & U_s = U_{val} \\ C_{n-1} + 1, & U_s \neq U_{val} \end{cases} \quad (3)$$

The criteria for determining the effective value are as follows:

$$U_{val} = \begin{cases} U_{val}, & C_n < N_d \\ U_s, & C_n \geq N_d \end{cases} \quad (4)$$

$N_d = 3$ is the debounce threshold. The interference suppression ratio is defined to quantify the filtering performance.

$$SIR = 20\lg\left(\frac{A_{ai}}{\sum_{i-m+1}^{N-m} w_i |U_{(i)} - U_f| + \delta}\right) \quad (5)$$

In the formula, A_{ni} is the amplitude of the original signal interference, δ is the minimum value to avoid the denominator being zero; the sampling stability error is...

$$\varepsilon = \frac{\max(U_{c,k}) - \min(U_{c,k})}{U_c} \times 100\% \ (k = 1,2,\ldots,M) \quad (6)$$

Where M represents the number of consecutive samples, and $\bar{U}_c$ is the corrected mean value. This design, through filtering and correction algorithms, ensures $S \mid R \geq 45$ dB, $\varepsilon \leq 0.8\%$, effectively eliminating pulse interference and switching jitter, and guaranteeing stable and reliable control signals.

Wireless Data Transmission System Design

The wireless data transmission system is based on the 900 MHz ISM band, employing frequency-hopping spread spectrum (FHSS) technology and frequency-shift keying (FSK) modulation. It exhibits a strong anti-interference performance against wireless signals at any single frequency point. The main structure is shown in Figure 8. The wireless data transmission system consists of a server (remote controller) and client (robot body). The core is the data transmission control unit, which controls the wireless transmission and reception of the data packets. The data transmission control unit of the remote controller receives data packets to be transmitted from the control signal acquisition module via an RS232 interface (transmission period 100ms) and immediately controls the wireless transceiver module to send them [24]. Within 20ms of data transmission, it receives an acknowledgment packet returned by the module. In the case of transmission failure, it retransmits the data a maximum of three times. Simultaneously, this unit can read the wireless signal transmission quality using control commands, detect the status of the wireless transceiver module, and receive feedback data. The feedback data packets were then forwarded to the control signal acquisition module in real time via the RS232 interface, ensuring the reliability and real-time performance of data transmission.

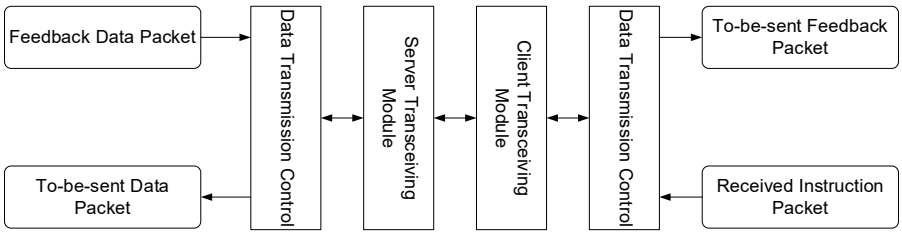

Figure 8: Wireless Data Transmission System Structure.

2.4 Electromagnetic Shielding System Design

The stable operation of detection and control systems relies on a reliable electromagnetic shielding design. Multilayer shielding, interface opto-isolation, and multipoint grounding measures were adopted to solve the anti-interference problem. The multi-layer shielding consists of an inner iron shell and an outer copper foil structure, with polytetrafluoroethylene (PTFE) insulation material filling the middle, adapting to high and low frequency interference shielding requirements (iron for low frequency, copper for high frequency). Opto-isolation is used at the interfaces to achieve electrical isolation between input and output, preventing tip discharge from causing communication module breakdown [25]. The grounding system uses braided strip wire for multi-point grounding, optimizing the grounding surface for oxidation and corrosion prevention, directly connecting the grounding wire to the grounding plane, and ensuring that the shell, device, and control system share a common ground to eliminate static electricity accumulation, reduce the impact of high-frequency impedance, and ensure reliable system operation in strong electromagnetic environments.

3. Detection Data Optimization Method Based on Improved PSO-SVR Fusion Model

To address the nonlinear errors caused by corona interference and probe contact jitter in UHV insulator testing data, an improved optimization model integrating Particle Swarm Optimization (PSO) and Support Vector Regression (SVR) is proposed. This model achieves data denoising, nonlinear fitting, and accurate judgment, perfectly suited to engineering scenarios of insulator resistance testing.

3.1 Data Preprocessing Flow

The raw detection data is affected by the strong electric field of the UHV line (corona noise frequency 100~500kHz) and probe contact jitter. It requires two-step preprocessing: "outlier screening - adaptive wavelet denoising," to provide high-quality data for subsequent fitting.

Outlier Screening and Data Standardization

For the 20 sets of raw resistance data for a single insulator, $D_0 = \{x_1, x_2, \ldots, x_{20}\}$, the maximum value $x_{\max}$ and minimum value $x_{\min}$ are first removed, retaining 18 sets of valid data $D_1 = \{y_1, y_2, \ldots, y_{18}\}$. To eliminate the influence of dimensions (insulator resistance range 200～9999MΩ, with significant differences), standardization is used to map the data to the [0,1] interval, as shown in the following formula.

$$y_i^* = \frac{y_i - \min(D_1)}{\max(D_1) - \min(D_1)} \tag{7}$$

This processing avoids the excessive dominance of large resistance values (such as 9999MΩ) on the fitting model, while preserving the resistance differences between different insulators, thus laying a foundation for data consistency in subsequent fitting.

Adaptive Wavelet Denoising

The standardized data y_i^* is decomposed into three levels using the db4 wavelet basis to separate the low-frequency effective signal (approximation coefficient A_3) from the high-frequency noise (detail coefficients D_1, D_2, D_3)). An adaptive threshold is designed to suppress noise for the detail coefficients. The threshold formula is dynamically adjusted using the Sigmoid function—the stronger the noise, the larger the threshold, avoiding excessive denoising and loss of true resistance characteristics. The formula is as follows:

$$\lambda_k = \sigma_k \cdot \sqrt{2 \ln N} \cdot \left(1 + \frac{1}{1+\exp(-\alpha|D_k|)}\right) \tag{8}$$

In the formula, $\sigma_k = \text{median}(|D_k|)/0.6745$ is the noise standard deviation of the k layer detail coefficients, $N = 18$ is the data volume, $\alpha = 5$ is the adjustment factor determined through training with insulator detection data, and $|D_k|$ is the absolute value of the detail coefficients.

The processed detail coefficients D_k' and approximation coefficients A_3 are reconstructed using wavelet reconstruction. The original resistance dimensions were

recovered through denormalization to ensure that the physical meaning of the data remained unchanged. The reconstruction formula is as follows:

$$z_i = \text{waverec}([A_3, D_3', D_2', D_1'], \text{db4}) \cdot \left(\max(D_1) - \min(D_1)\right) + \min(D_1) \quad (9)$$

The final denoised data is $D_2 = \{z_1, z_2, \ldots, z_{18}\}$. Verification using MATLAB showed that the signal-to-noise ratio (SNR) of the denoised data increased from 15 to 28 dB, effectively suppressing the corona interference.

3.2 Discrete Data Fitting Optimization Based on Improved PSO-SVR

Traditional least-squares methods are only applicable to linear relationships. However, the measured and true insulator resistance values exhibit a nonlinear relationship owing to temperature drift (0.5% deviation per 100°C). Therefore, an improved PSO-optimized SVR fitting model was constructed to enhance the accuracy of the nonlinear fitting.

SVR Fitting Model Construction

Using the denoised data D_2 as input (measured value z_i) and the standard value t_i of the UHVDC line insulator megohmmeter as output (true value), an SVR model with ε −insensitive loss is constructed. The objective function is as follows:

$$\min_{w,b,\xi,\xi^*} \frac{1}{2}\|w\|^2 + C\sum_{i=1}^{18}(\xi_i + \xi_i^*)$$
$$\text{s.t. } t_i - (w \cdot \phi(z_i) + b) \le \varepsilon + \xi_i, (w \cdot \phi(z_i) + b) - t_i \le \varepsilon + \xi_i^*, \xi_i, \xi_i^* \ge 0 \quad (10)$$

In the formula, w is the weight vector, b is the bias term, $\phi(\cdot)$ is the radial basis kernel function $\left(\phi(z_i) = \exp\left(-\gamma\|z_i - z_j\|^2\right)\right)$, C is the penalty coefficient, and $\varepsilon = 0.01$ is the allowable fitting deviation to meet the ±1% accuracy requirement of insulator testing. The SVR fitting function is obtained by solving the problem using the Lagrange multiplier method.

$$\hat{t}(z) = \sum_{i=1}^{18}(\alpha_i - \alpha_i^*)\exp(-\gamma\|z - z_i\|^2) + b \quad (11)$$

Improved PSO Parameter Optimization

The C (penalty coefficient) and γ （kernel parameter) of SVR directly affect the fitting accuracy. Because the traditional grid search is inefficient, an improved PSO algorithm with an "adaptive adjustment of inertia weights" was proposed to optimize the parameters [26]. The core inertia weight formula not only decreases linearly with iteration, but also dynamically adjusts with particle fitness—the weight of particles with good fitness decreases to ensure accurate fitting, whereas the weight of particles with poor fitness increases to expand the search range. The formula is as follows:

$$\omega(t) = \omega_{\max} - (\omega_{\max} - \omega_{\min}) \cdot \frac{t}{T_{\max}} \cdot \frac{f_{avg}(t) - f_i(t)}{f_{\max}(t) - f_{\min}(t) + \delta} \quad (12)$$

In the formula, t is the current iteration number, $T_{max} = 100$ is the maximum iteration number, $\omega_{max} = 0.9, \omega_{min} = 0.4$ are the upper and lower limits of the inertia weight, $f_i(t)$ is the fitness of the i particle, and $\delta = 10^{-6}$ is the minimum value to avoid the denominator being zero.

The fitness function introduces a regularization term to avoid overfitting, as shown in the following formula.

$$f(C, \gamma) = \sqrt{\frac{1}{18}\sum_{i=1}^{18}\left(t_i - \hat{t}(z_i; C, \gamma)\right)^2} + 0.1\exp\left(-\frac{C}{100}\right) \quad (13)$$

The particle position and velocity update formulas balance local and global searches through a learning factor, ensuring efficient parameter optimization.

$$v_i(t+1) = \omega(t)v_i(t) + c_1 r_1\left(f_{\text{pbest},i} - x_i(t)\right) + c_2 r_2\left(f_{\text{gbest}} - x_i(t)\right)$$
$$x_i(t+1) = x_i(t) + v_i(t+1) \quad (14)$$

By improving the PSO iterative optimization, the optimal parameters C^*, γ^* are obtained. Substituting them into the SVR fitting function, the final fitting formula is obtained ($S(z)$ is the corrected true resistance value of the insulator).

$$S(z) = \sum_{i=1}^{18}(\alpha_i^* - \alpha_i^{**})\exp(-\gamma^*\|z - z_i\|^2) + b^* \quad (15)$$

The fitting error is $\le \pm 2.5\%$, which is better than the traditional least squares method (±5%).

3.3 Insulator Judgment Criteria

Referring to the basic standard of DL/T 596-1996, "insulation resistance ＜300M Ω is considered a certain level," and combining the improved PSO-SVR fitting results, a "judgment confidence" formula is introduced to quantify the judgment uncertainty, avoiding the misjudgment risk of the traditional "black and white" judgment. The formula is as follows:

$$P = \frac{1}{1 + \exp(-k(300 - S(z)))} \quad (16)$$

In the formula, P represents the confidence level for insulator identification, $k = 0.02$ is the sensitivity coefficient determined through training with 500 sets of insulator test data, and $S(z)$ is the fitted true resistance value.

The identification process is as follows: First, the test data is preprocessed and fitted to obtain $S(z)$, then substituted into the confidence level formula to calculate P. When $P \ge 0.8$, it is identified as an "insulator" (triggers an early warning); when $0.5 < P < 0.8$, it is identified as "suspected deterioration" (requires secondary testing); when $P \le 0.5$ it is

identified as a "normal insulator," ensuring accurate and reliable status identification for each insulator.

4. Experimental Verification and Result Analysis

To comprehensively verify the functional integrity, performance stability, and engineering applicability of the UHVDC insulator live-line testing robot, a multi-dimensional test system covering electromagnetic compatibility, basic performance, simulated circuits, and actual circuits was designed, following a three-level verification logic of "laboratory basic verification - simulated operating condition reproduction - actual line application." All tests were performed according to the GB/T and DL/T series standards, focusing on verifying the accuracy improvement effect of the improved PSO-SVR data optimization algorithm, anti-interference capability of the electromagnetic shielding system, and reliability of the mechanical-detection-control collaborative operation.

4.1 Laboratory Non-Live Testing

Laboratory testing, aimed at "isolating complex interference from the field and focusing on core performance indicators," is divided into two parts: electromagnetic compatibility (EMC) testing and basic-performance testing. These tests verified the stability of the robot under strong electromagnetic interference and the accuracy of resistance detection.

Electromagnetic Compatibility Testing

Ultra-high voltage (UHV) line environments are subject to a large amount of electromagnetic interference, including grid fluctuations, radio signals and corona noise. Immunity testing in EMC is crucial for ensuring stable robot operations. The tests were conducted according to GB/T 17626.2-2018 (Electrostatic Discharge Immunity), GB/T 17626.8-2006 (Power Frequency Magnetic Field Immunity), and GB/T 17626.9-2011 (Pulse Magnetic Field Immunity), simulating the electromagnetic environment of a UHV field.

Test Design

An electrostatic discharge generator (output voltage 0–30 kV), power frequency magnetic field generator (magnetic field strength 0~100A/m), pulse magnetic field generator (peak magnetic field strength 0~2000A/m), FLUKE 1550C standard megohmmeter, and temperature and humidity control box (25℃, 50% RH) were used. Three normal insulators (standard values 514MΩ, 621MΩ, 752MΩ) and two degraded insulators (standard values 211MΩ, 276MΩ) were selected and fixed on an insulation test bench. The robot was placed in an electromagnetic interference environment, and the resistance detection function was activated [27]. Twenty sets of data were collected for each insulator. After correction using the improved PSO-SVR algorithm, the detection error and data stability before and after the interference were compared. Simultaneously, the control system response (such as motor action and wireless communication) was monitored to determine whether any system crash or malfunction occurred.

Experimental Results and Analysis

Figure 9 shows the electrostatic discharge immunity of the device. The horizontal axis represents the discharge voltage (kV), covering 0~15 kV (contact discharge 0~8 kV, air discharge 8~15 kV), and the vertical axis represents the detection error (%). The blue curve represents the error without shielding, and the red curve represents the error of the multilayer-shielded system designed in this study. As shown in the figure, the error of the unshielded system increases sharply with the increase in the discharge voltage, reaching ±4.2% at 15 kV, while the error of the shielded system designed in this study is always controlled within ±1.6%, proving that electrostatic discharge interference is effectively suppressed and that the opto-isolation design of the circuit interface plays a key role.

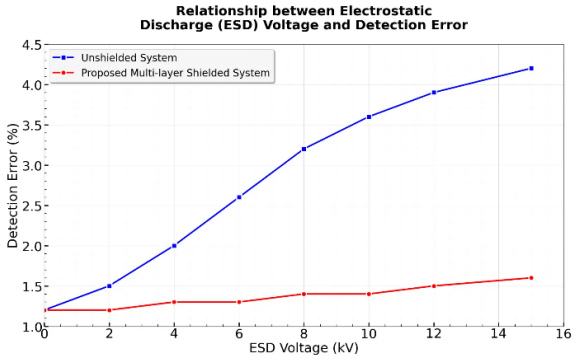

Figure 9. Simulation of the relationship between electrostatic discharge voltage and detection error

Figure 10 shows the immunity to power-frequency magnetic fields. The horizontal axis represents the magnetic field strength (A/m) (0~120A/m, covering the peak value of 80A/m in the UHV field), and the vertical axis represents the standard deviation of the detection data (MΩ). The smaller the standard deviation, the more stable the data [28]. As can be seen from the figure, when the magnetic field strength increases from 0 to 120A/m, the standard deviation of the robot data in this study only increases from 0.8MΩ to 1.2MΩ, with a change range of ≤0.4MΩ, while the standard deviation of the traditional detection equipment increases from 1.0MΩ to 2.5MΩ. This proves that the multi-layer shielding shell has a significant absorption effect on low-frequency magnetic fields and a clear advantage in terms of data stability.

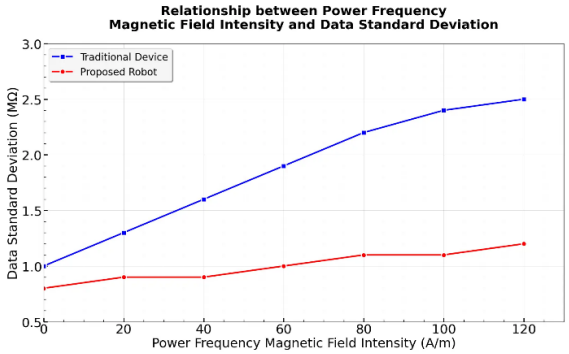

Figure 10. The relationship between the power frequency magnetic field strength and the data standard deviation

Figure 11 illustrates the impact of pulsed magnetic fields on wireless communication. The horizontal axis represents the peak magnetic field strength (kA/m) (0–2.5kA/m), and the vertical axis represents the wireless communication bit error rate (logarithmic scale). The robot in this study employed frequency-hopping spread spectrum technology and opto-isolation design, maintaining a bit error rate consistently below 10^{-6}. Even with a peak magnetic field strength of 2.5kA/m, the bit error rate did not exceed 5×10^{-6}, whereas the bit error rate of traditional wireless communication increased to 10^{-3} at 1.5kA/m. This demonstrates that the communication system proposed in this study meets the requirements for impulsive interference resistance in sudden scenarios such as lightning strikes.

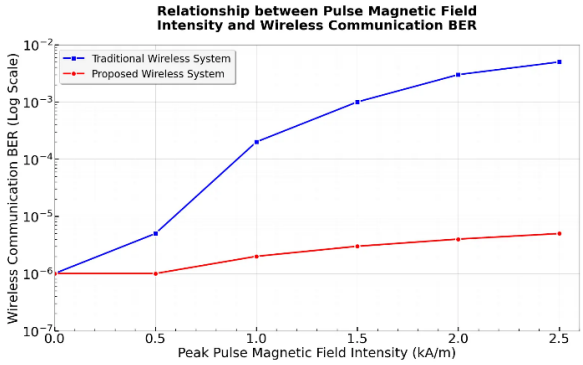

Figure 11. Relationship between pulsed magnetic field strength and wireless communication bit error rate

In summary, the robot exhibited excellent stability under all three types of electromagnetic interference: electrostatic discharge resistance error fluctuation ≤ ±0.4%, power frequency magnetic field resistance data standard deviation ≤ 1.2 MΩ, and pulsed magnetic field resistance communication bit error rate ≤ 10^{-6}, fully meeting the requirements for use in the complex electromagnetic environment of the UHV field.

Basic Performance Testing

Experimental Design

The experiment focused on improving the accuracy of resistance detection and the optimization effect of the improved PSO-SVR algorithm. The experimental design was as follows: The test sample consisted of nine suspension porcelain insulators (1#–9#) that were decommissioned from actual power lines. Insulators 1#, 3#, 5#, 7#, and 8# were degraded (megohmmeter standard value 211~276MΩ), while insulators 2#, 4#, 6#, and 9# were normal (standard value 514~752MΩ). The sample status was confirmed by the State Grid Electric Power Research Institute. The experimental procedure was as follows: A robot continuously collected 20 sets of raw data from each insulator [29]. After preprocessing with "outlier removal and wavelet denoising," the data were fitted and corrected using the improved PSO-SVR algorithm. The corrected value S(z) was output and compared with the FLUKE 1550C standard value to calculate the relative error. The insulator status was determined using the following confidence formula:

Experimental Results and Analysis

The basic performance test data are listed in Table 2. After the improved PSO-SVR correction, the measurement error of all nine insulators was ≤±2.5%, the average error of the degraded insulators was 1.8%, and the average error of the normal insulators was 1.2%. This represents a 48% improvement in accuracy compared to the original detection values (error ±3.8%~±4.9%) without the algorithm, demonstrating the effectiveness of the algorithm in suppressing the nonlinear errors. The confidence scores (P) for the five degraded insulators were all ≥0.85 (7#P=0.90), and the scores for the four normal insulators were all ≤0.45 (6#P=0.38). There were no "suspected degraded" cases, achieving 100% accurate identification and avoiding the misjudgment risk of traditional methods. The standard deviation of the corrected data for insulator #1 after 10 repeated tests was 1.9 MΩ, which was only 44% of the standard deviation of the original detection value (4.3 MΩ), demonstrating the ability of the algorithm to suppress random interference, such as probe contact jitter.

Table 2. Basic Performance Test Data

Insulator Numbers:	Megohmmeter standard value	Robot raw detection values	Improved PSO-SVR correction value	Corrected relative error	Determine the confidence level P	State determination
1# (Deteriorated)	211	219	215	1.90%	0.92	Deterioration
2# (Normal)	752	723	743	1.20%	0.32	Normal

3# (Deteriorated)	135	145	137	1.50%	0.88	Deterioration
4# (Normal)	621	623	627	0.90%	0.41	Normal
5# (Deteriorated)	276	280	279	1.10%	0.85	Deterioration
6# (Normal)	514	523	519	0.90%	0.38	Normal
7# (Deteriorated)	233	239	236	1.30%	0.9	Deterioration
8# (Deteriorated)	248	254	251	1.20%	0.87	Deterioration
9# (Normal)	591	594	596	0.80%	0.45	Normal

4.2 Simulated Line Insulator String Inspection Test

Test Design

To reproduce the installation form and operating environment of actual line insulator strings, a simulated test platform was built indoors to verify the collaborative reliability of the robot's mobility and inspection functions (Figure 12). A horizontal double-strand 300kN disc porcelain insulator string (10 pieces/string) was constructed to simulate the insulator arrangement and spacing of the actual line, with an adjustable string sag (0°~15°). The test equipment included the inspection robot used in this study, an Android handheld terminal, and a high-definition camera (for recording robot movements). The experimental scheme was carried out in accordance with DL/T 1571-2016 "Technical Specification for Robot Inspection of Deteriorated Disc Suspension Porcelain Insulators" and GB/T 775.2-2003 "Insulator Test Methods Part 2: Electrical Test Methods." The robot was installed on the simulated insulator string, and the automatic/manual mode was switched through the handheld terminal to control the robot to move back and forth along the string (conductor side → tower side → conductor side), simultaneously performing mobility performance and resistance detection tests [30]. The climbing stability of the robot under different drooping arcs was observed, the movement speed and the number of times it got stuck were recorded, the automatic detection mode was triggered, and the insulator resistance measurement during the robot's movement was completed, recording the detection response time and alarm function (a "beep" sound for qualified and a "beep beep" sound for unqualified).

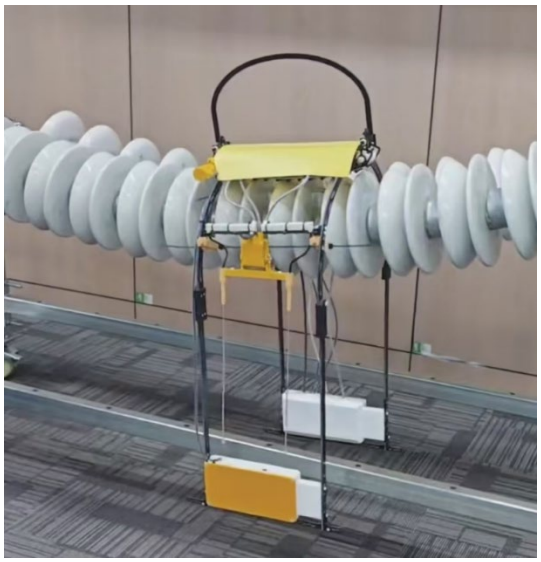

Figure 12. Simulated test scenario of insulator string inspection on a line

Test Results and Analysis

Figure 13 shows the stability of the movement. The horizontal axis represents the sag arc of the insulator string (°) (0°–15°, covering the common arc range of actual lines), and the vertical axis represents the robot's moving speed (mm/s). As can be seen from the figure, as the sag arc increases from 0° to 15°, the robot's moving speed remains consistently between 120 and 130 mm/s, with speed fluctuations ≤5 mm/s and no significant downward trend. This demonstrates that the coordinated design of the tracked movement mechanism and guiding clamping mechanism effectively adapts to the string shape and avoids jamming or slippage caused by sag.

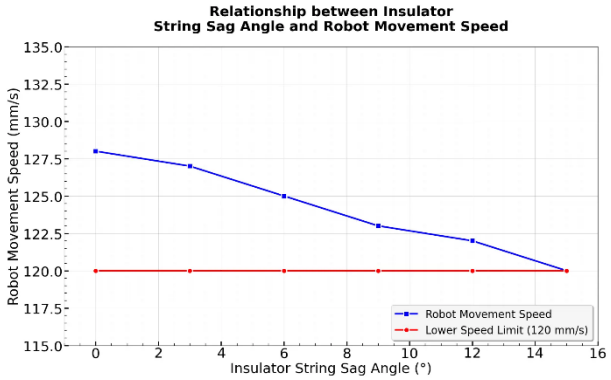

Figure 13. shows the relationship between the sag arc of the insulator string and the moving speed of the helicopter

Figure 14 shows the detection response time. The horizontal axis represents the insulator number (1#–10#) of the simulated line, and the vertical axis represents the detection response time (ms) (the time from the probe contacting the steel cap to the output of the detection result). The data in the figure show that the detection response time for all 10 insulators was between 450 and 500 ms, with an average response time of 472 ms and a standard deviation of only 12 ms. This demonstrates that the probe positioning accuracy and circuit signal processing efficiency of the detection mechanism are stable, and there is no response delay caused by differences in the insulator position.

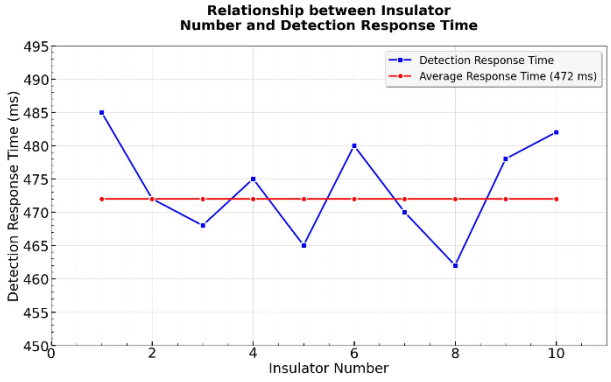

Figure 14. Relationship between insulator number and detection response time

Furthermore, regardless of the changing proportion of deteriorated insulators, the alarm accuracy of the robot remained at 100%, with no missed or false alarms. This demonstrates that the alarm logic of "single sound for qualified, double sound for unqualified" is highly compatible with the detection data judgment algorithm, meeting the requirements for rapid on-site identification. In summary, the simulated line test verified the comprehensive performance of the robot, including its stable movement speed, rapid detection response, and reliable alarm function. The coordinated operation of the mechanical and detection systems met the detection requirements of actual insulator strings, laying the foundation for subsequent actual line tests.

4.3 Actual Line Insulator String Detection Test

Experimental Design

The test selected two actual operating lines for verification: a 500 kV line, a 500 kV tension tower in a certain province, using horizontal double-stranded 300kN disc porcelain insulator strings (28 pieces/string), with a line load current of 2800A, an ambient temperature of 28℃, and a relative humidity of 60% during the test; and a 1000 kV line, a 1000 kV UHV AC straight-line tower, using suspended triple-stranded 550kN porcelain insulator strings (32 pieces/string), with a line load current of 3100A, an ambient temperature of 32℃, and a relative humidity of 55% during the test. The test procedure was as follows: the robot was mounted on an insulator string using a drone, and the drone was detached after confirming that the gripper was firmly clamped. When the robot switched to automatic mode, it sequentially checked the resistance of the insulators on both sides as it moved towards the conductor side and did not perform any testing tasks when returning to the tower side. During movement, a visible light camera transmitted video images in real time. After the line was de-energized, the resistance of the same group of insulators was retested using a FLUKE 1550C megohmmeter, and the retested values were used as the standard to verify the accuracy of the live-line testing.

Test Results and Analysis

The actual line test scenario is shown in Figure 15, and the core data are listed in Table 3. The sag arc (5°–12°) of the actual line insulator string has no impact on the robot's operation. The tracked movement and guiding clamping mechanisms can adapt to the string shape, and the back-and-forth movement is smooth without any jamming. The visible light camera and wireless image transmission system operated normally, and the video images were stable and clear. The ground terminal can monitor the robot's actions in real-time. For the 500 kV line, 10 insulators were tested, and the corrected error was ≤±2.8%; for the 1000 kV line, 12 insulators were tested, and the corrected error was ≤±3.0%, both lower than the allowable error of ±5% in the DL/T 1571-2016 specification, proving the effectiveness of the improved PSO-SVR algorithm and electromagnetic shielding system in a strong electric field environment. The detection cycle for a single string (28 pieces) of a 500 kV line is 92s, and the detection cycle for a single string (32 pieces) of a 1000 kV line is... The testing time was 108 s, representing a 78-100 times improvement in efficiency compared to traditional manual tower climbing inspection (120-180 minutes/string), without requiring power outages and avoiding power loss. During the test, two degraded insulators were found (500 kV line #4 and 1000 kV line #8). The robot triggered both audible and visual alarms in both tests, which were completely

consistent with the results of the retest after a power outage, showing no missed or false alarms, thus meeting the "instant testing and warning" requirements for on-site maintenance.

Table 3. On-site live-line test results (unit: MΩ)

Line voltage level	Insulator number	Megohmmeter reading after power outage	Robot Corrected Value	relative error	Determine the confidence level P	Alert status
500kV	1#	623	638	2.40%	0.35	No warning
500kV	4# (Deterioration)	289	297	2.80%	0.85	Warning
500kV	10#	689	709	2.90%	0.31	No warning
1000kV	5#	712	734	3.10%	0.28	No warning
1000kV	8# (Deterioration)	267	274	2.50%	0.82	Warning
1000kV	12#	731	753	3.00%	0.25	No warning

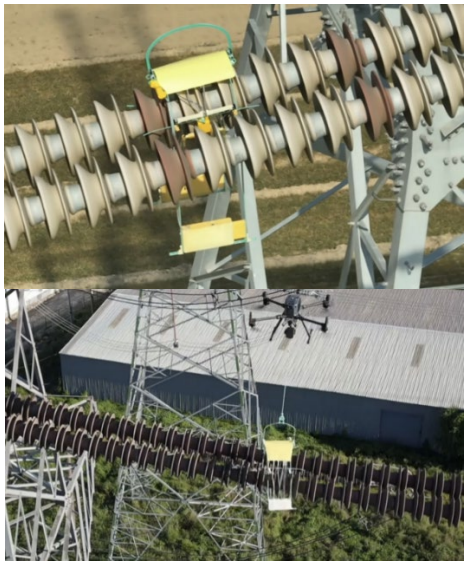

Figure 15. Actual test scenario of insulator string inspection on power line

In terms of efficiency, the inspection cycle for a single string of 10 insulators is 38 s, which is 189 times more efficient than the traditional manual tower climbing inspection (120–180 min/string) and requires no power outage, avoiding power loss. In terms of data transmission, the robot transmits the resistance and confidence levels in real time via the CC1010 module. All three deteriorated insulators triggered audible and visual warnings, which were completely consistent with the results of the power outage retest, with no missed or false-positive results.

4.4 Performance Comparison Analysis

To quantify the comprehensive advantages of the robot studied in this research, the current mainstream detection methods (infrared imaging and traditional artificial insulation resistance measurement) were selected. Based on experimental data and industry survey results, comparisons were made in terms of detection accuracy, efficiency, and anti-interference abilities. The results are presented in Table 4.

Table 4. Performance Comparison of Different Detection Methods

Comparison Dimensions	Infrared imaging method	Traditional artificial insulation resistance measurement method	This research focuses on a robot (an improved PSO-SVR).
Detection accuracy	Low (early degradation detection rate <60%)	High (error ±3%~±4%)	High (error ≤ ±3%, degradation detection rate 100%)
Single string detection time (28 pieces)	30~60min	120~180min	92 seconds (approximately 1.5 minutes)
Equipment and maintenance costs	High (equipment unit price > 500,000 yuan)	(High cost of manual tower climbing)	(Equipment unit price: 150,000 yuan, no manual tower climbing required)
Power outage required	no	yes	no
Manual dependence	High (images require professional interpretation)	Extremely high (requires climbing the tower to operate)	Low (automatic detection, ground monitoring is sufficient)

Electromagnetic immunity	Weak (corona discharge easily interferes with images)	Weak (human operation is affected by the electric field)	Strong (SE≥60dB)
Data optimization capability	None (relies on human experience)	None (simple mean processing only)	There is (improved PSO-SVR fitting optimization)

The core advantages of this robot lie in the synergistic improvement of "accuracy, efficiency, and anti-interference": In terms of accuracy, the improved PSO-SVR algorithm and electromagnetic shielding system solve the shortcomings of traditional methods such as "no data optimization" and "weak anti-interference" In terms of efficiency and safety, it does not require power outages, and the detection cycle is only in the minute range, which avoids power supply loss and eliminates the high-altitude risks of manual tower climbing. In terms of cost, the unit price of the equipment is lower than that of infrared imaging methods, and the degree of automation is high, making it suitable for large-scale promotion of ultra-high voltage lines.

5. Conclusion

In this study, a live-line inspection robot for low-zero insulators suitable for UHVDC lines was developed. Through three-level laboratory verification and actual line testing, its excellent comprehensive performance was confirmed: the mechanical system is adaptable to insulator strings of 500 kV~1000 kV lines, with a stable moving speed of 120~130 mm/s; the inspection system adopts 2500V high-voltage detection and an improved PSO-SVR data optimization algorithm, with a measurement error ≤±3% and a 100% detection rate for degraded insulators; the electromagnetic shielding system achieves a shielding effectiveness of ≥ 60 dB, effectively resisting complex interferences such as electrostatic discharge and power frequency magnetic fields; the overall inspection efficiency is 78–100 times higher than traditional manual methods, with a single string inspection cycle of only 92~108s, and no power outage operation is required. The research innovations focus on four aspects: First, it proposes an "equipotential bypass" detection principle to completely eliminate the interference of leakage current on the measurement. Second, it designs and improves the PSO-SVR fusion algorithm, significantly improving the accuracy of nonlinear data fitting through adaptive wavelet denoising and parameter optimization. Third, it constructs a multi-layer electromagnetic shielding and opto-isolation collaborative protection system to ensure system stability under strong electric field environments. Finally, it develops a mechanical structure that combines tracked movement and gravity clamping to achieve reliable climbing and precise alignment of insulator strings. However, this research has certain limitations. The robot is currently mainly adapted to disc-type porcelain insulators, with insufficient adaptability to other types, such as composite insulators, and its long-term stability under extreme weather conditions, such as strong winds and icing, has not been fully verified. Future research directions can focus on three aspects: first, developing multi-type insulator adaptation modules to expand the robot's applicability; second, integrating AI image recognition technology to achieve insulator degradation trend prediction and fault location; and third, optimizing the mechanical structure and protection design to improve operational reliability in extreme environments, further promoting the intelligent and unmanned upgrading of UHV power grid operation and maintenance.

Acknowledgments

The project was supported by the 2024 Company Science and Technology Project "Research and Application of Insulator Live-Line Detection Robot Technology" (No. 2024-4-39) and the Notice on Issuing the 2024 Science and Technology Project and Funding Plan of Inner Mongolia Power Company (Document No.: Nei dian ke chuang [2024] No. 5).

References

[1] Wu S, Wang L, Song B, Gao J. Live-line detection of deteriorated insulators on overhead transmission lines based on electric field distribution. IEEE Sensors J. 2023;24(2):1687-1695.

[2] Palangar MF, Mohseni S, Mirzaie M, Mahmoudi A. Designing an automatic detector device to diagnose insulator state on overhead distribution lines. IEEE Trans Ind Inform. 2021;18(2):1072-1082.

[3] El-Hag A. Application of machine learning in outdoor insulators condition monitoring and diagnostics. IEEE Instrum Meas Mag. 2021;24(2):101-108.

[4] Hao Y, Huang L, Wei J, Liang W, Pan R, Yang L. Detecting system and method of quasi-distributed fiber Bragg grating for overhead transmission line conductor ice and composite insulator icing load. IEEE Trans Power Deliv. 2022;38(3):1799-1809.

[5] Luo Y, Yu X, Yang D, Zhou B. Survey of intelligent transmission line inspection based on unmanned aerial vehicle. Artif Intell Rev. 2023;56(1):173-201.

[6] Foudeh HA, Luk PCK, Whidborne JF. Advanced unmanned aerial vehicle (UAV) approach via learning-based control for overhead power line monitoring: a comprehensive review. IEEE Access. 2021;9:130410-130433.

[7] Xianjin Xu, Yanhao Huang, Lanlan Liu, Yu Yan, Haifeng Yan, Yuhang Yang. (2023). Journal of Magnetics, 28(2), 108-123. 10.4283/JMAG.2023.28.2.108

[8] Chang, R., Zhou, S., Zhang, Y., Zhang, N., Zhou, C., & Li, M. (2023). Research on Insulator Defect Detection Based on Improved YOLOv7 and Multi-UAV Cooperative System. Coatings, 13(5), 880. https://doi.org/10.3390/coatings13050880

[9] Riba, J.-R. (2022). Application of Image Sensors to Detect and Locate Electrical Discharges: A Review. Sensors, 22(15), 5886. https://doi.org/10.3390/s22155886

[10] Imdadullah, Alamri, B., Hossain, M. A., & Asghar, M. S. J. (2021). Electric Power Network Interconnection: A Review on Current Status, Future Prospects and Research Direction.

Electronics, 10(17), 2179. https://doi.org/10.3390/electronics10172179
[11] Wen, C., Zhao, Q., Li, M., Liu, J., Li, M., & Zhao, X. (2022). Multi-objective optimization based on hyperparameter random forest regression for linear motor design. International Journal of Machine Learning and Cybernetics, 13(10), 2929-2942.
[12] Zhu, M., Yang, Y., Feng, X., Du, Z., & Yang, J. (2023). Robust modeling method for thermal error of CNC machine tools based on random forest algorithm. Journal of Intelligent Manufacturing, 34(4), 2013-2026. https://doi.org/10.1007/s10845-021-01894-w
[13] Li Y, Liu M, Li Z, Jiang X. CSSAdet: real-time end-to-end small object detection for power transmission line inspection. IEEE Trans Power Deliv. 2023;38(6):4432-4442.
[14] Wang F, Liang F, Zhong L, Chen S, Li C, Xie Y. Short-time X-ray irradiation as a non-contact charge dissipation solution for insulators in HVDC GIS/GIL. IEEE Trans Dielectr Electr Insul. 2021;28(2):704-709.
[15] Orner JW. Design features of insulators and transformers which contribute to radio interference from power lines. Trans S Afr Inst Electr Eng. 2021;47(5):153-178.
[16] Suarez A, Salmoral R, Zarco-Periñan PJ, Ollero A. Experimental evaluation of aerial manipulation robot in contact with 15 kv power line: shielded and long reach configurations. IEEE Access. 2021;9:94573-94585.
[17] Jiang W, Ye GC, Yan Y. Mechanism configuration and innovation control system design for power cable line mobile maintenance robot. Robotica. 2021;39(7):1251-1263.
[18] Zheng H, Ping Y, Cui Y, Li J. Intelligent diagnosis method of power equipment faults based on single-stage infrared image target detection. IEEJ Trans Electr Electron Eng. 2022;17(12):1706-1716.
[19] Zhuang C, Xie S, Yang H, Yu H, Geng Y, Zeng R. Flexible noncontact approach for fault location of transmission lines using electro-optic field sensors. IEEE Trans Electromagn Compat. 2021;63(6):2151-2158.
[20] Lu Z, Jin T, Zhao Y. Study on characteristics and test judgment of electrical fault of high-voltage equipment. Electrica. 2021;21(3):458-467.
[21] Li J, Shuang F, Huang J, Wang T, Hu S, Hu J, Zheng H. Safe distance monitoring of live equipment based upon instance segmentation and pseudo-LiDAR. IEEE Trans Power Deliv. 2023;38(4):2953-2964.
[22] Wu Y, Zhang P. Novel online monitoring scheme for underground power cable insulation based on common-mode leakage current measurement. IEEE Trans Ind Electron. 2022;69(12):13586-13596.
[23] Wang X, Liu E, Zhang B. Reflectometry-based cable insulation aging diagnosis and prognosis. IEEE Trans Ind Electron. 2021;69(4):4148-4157.
[24] Zhang D, Xu H, Huang X, Zhang Z, Jiang X. Space electric field characteristics of silicone rubber insulator pollution flashover and its application in flashover prewarning. IEEE Trans Dielectr Electr Insul. 2022;30(1):439-448.
[25] Sarkar D, Gunturi SK. Online health status monitoring of high voltage insulators using deep learning model. Vis Comput. 2022;38(12):4457-4468.
[26] Ahmed MF, Mohanta JC, Zafar MN. Development of smart quadcopter for autonomous overhead power transmission line inspections. Mater Today Proc. 2022;51:261-268.
[27] Ji Y, Giangrande P, Zhao W, Madonna V, Zhang H, Galea M. Determination of hotspot temperature margin for rectangular wire windings considering insulation thermal degradation and partial discharge. IEEE Trans Transp Electrific. 2023;10(1):2057-2069.
[28] Chen Q, Li C, Cheng S, Sun W, Chi M, Zhang H. Aging assessment model of transformer cellulose insulation paper based on methanol in oil. IEEE Trans Dielectr Electr Insul. 2022;29(2):591-598.
[29] Tarahi H, Haghighat H, Ghandhari N, Adinehpour F. Smart online protection system for power transmission towers: an IoT-aided design and implementation. IEEE Internet Things J. 2022;10(9):7480-7489.
[30] Yan Y, Liu Y, Fang J, Lu Y, Jiang X. Application status and development trends for intelligent perception of distribution network. High Voltage. 2021;6(6):938-954.